AIAA JOURNAL
Vol. 43, No. 7, July 2005

Formation and Stability of Near Chapman–Jouguet Standing Oblique Detonation Waves

Giovanni Fusina*
Defence Research and Development Canada, Ottawa, Ontario K1A 0Z4, Canada
Jean P. Sislian†
University of Toronto, Downsview, Ontario M3H 5T6, Canada
and
Bernard Parent‡
Seoul National University, Seoul 151-744, Republic of Korea

A numerical investigation of the behavior of standing oblique detonation waves (ODWs) near the Chapman–Jouguet (minimum entropy) point is the main purpose of this investigation. The laminar, two-dimensional Navier–Stokes equations coupled with a nonequilibrium hydrogen–air combustion model based on chemical kinetics are used to represent the physical system. The equations are solved with the window allocatable resolver for propulsion computational fluid dynamics code (Parent, B., and Sislian, J. P., "The Use of Domain Decomposition in Accelerating the Convergence of Quasihyperbolic Systems," *Journal of Computational Physics*, Vol. 179, No. 1, 2002, pp. 140–169). A time-accurate simulation of the formation of a standing ODW near the Chapman–Jouguet condition yields a nonoscillatory, stable structure. The stability of the ODW to inhomogeneities in the oncoming fuel–air mixture is assessed through other time-accurate simulations by artificially introducing small disturbances consisting of pure air just upstream of the ODW structure. The ODW is shown to be resilient to these disturbances. The induction process and radical formation within the ODW structure are also analyzed.

Nomenclature

$\mathcal{A}$	=	coefficient used to calculate k_f
a	=	coefficient for thermochemical polynomial
c_P	=	specific heat at constant pressure
$\mathcal{D}$	=	mass diffusion coefficient
E	=	total energy
e	=	internal energy
$\mathcal{E}$	=	coefficient used to calculate k_f
$\boldsymbol{F}$	=	convection flux vector
$\boldsymbol{G}$	=	vector of diffusion variables
h	=	enthalpy (mass basis)
$\hat{h}$	=	molar enthalpy
J	=	metric Jacobian
K	=	diffusion matrix
K_c	=	equilibrium constant
k_b	=	backward reaction rate constant
k_f	=	forward reaction rate constant
M	=	Mach number
m	=	molecular weight
N_e	=	number of elementary reactions involving a species
N_l	=	number of species involved in an elementary reaction
n	=	coefficient used to calculate k_f
n_d	=	number of dimensions
n_s	=	number of species
P	=	pressure
$\boldsymbol{Q}$	=	vector of conserved variables
q	=	magnitude of the velocity vector
R	=	gas constant, residual
$\mathcal{R}$	=	universal gas constant
$\boldsymbol{S}$	=	vector of source terms
s^o	=	molar entropy at reference state
T	=	temperature
t	=	time
$\boldsymbol{V}$	=	contravariant velocity vector
$\boldsymbol{v}$	=	velocity vector
$\dot{\boldsymbol{W}}$	=	vector of species production terms (mass per unit time)
X	=	curvilinear coordinate
x	=	Cartesian coordinate
Y	=	mass fraction
y	=	Cartesian coordinate
α	=	metric term
β	=	metric term
δ	=	flow deflection angle
ΔG^o	=	difference in Gibbs free energy at reference state between products and reactants
δ_{ij}^{Kr}	=	Kronecker delta
ε	=	detonation wave angle
η	=	third-body efficiency
θ	=	flow angle
κ	=	thermal conductivity
μ	=	viscosity
ν'	=	stoichiometric coefficient for reactants
ν''	=	stoichiometric coefficient for products
ξ	=	convergence criterion
ξ_{verge}	=	user-defined convergence criterion threshold
ρ	=	density
ϕ	=	equivalence ratio
χ	=	mole fraction

Presented as Paper 2004-1125 at the AIAA 42nd Aerospace Sciences Meeting, Reno, NV, 5–8 January 2004; received 16 March 2004; revision received 1 December 2004; accepted for publication 31 January 2005. Copyright © 2005 by the authors. Published by the American Institute of Aeronautics and Astronautics, Inc., with permission. Copies of this paper may be made for personal or internal use, on condition that the copier pay the $10.00 per-copy fee to the Copyright Clearance Center, Inc., 222 Rosewood Drive, Danvers, MA 01923; include the code 0001-1452/05 $10.00 in correspondence with the CCC.

*Defence Scientist; giovanni.fusina@utoronto.ca. Member AIAA.
†Professor, Institute for Aerospace Studies; sislian@caius.utias.utoronto.ca. Associate Fellow AIAA.
‡Research Associate, Department of Aerospace Engineering; currently Visiting Research Fellow, Institute for Aerospace Studies, University of Toronto, Downsview, ON M3H 5T6, Canada; bernard.parent@utoronto.ca. Member AIAA.

Introduction

A SHOCK in a supersonic or hypersonic flow of a combustible mixture can raise the temperature and pressure of the mixture to values high enough to induce combustion. After a short ignition delay, where temperature and pressure remain nearly constant but the

concentration of radical species increases by orders of magnitude, exothermic reactions take place. If the heat release occurs sufficiently close to the shock, such that a coupled shock–flame front is formed, this phenomenon is termed a detonation wave.[1] In other words, a detonation is a shock-induced combustion process where the shock receives at least part of its support from the combustion. This support is transmitted along characteristics that emanate from the reaction site back to the shock.

Detonation waves can either propagate in a combustible mixture or be standing in a hypersonic flow of a combustible mixture over a wedge or blunt body. Propagating detonation waves can have multidimensional structures which are inherently unsteady, leading to complex shock–reaction front interactions termed *cellular structure of detonation waves*,[2,3] a phenomenon that has been studied at length in the past.[2,4,5]

For the case of a blunt-body-shaped projectile traveling at hypersonic speeds in a hydrogen–air mixture, both steady and unsteady detonation wave structures have been observed experimentally[6] and modeled at length computationally.[7–9]

We focus on standing detonation waves, specifically standing oblique detonation waves (ODWs) attached to a wedge, because these are of most interest for the purposes of hypersonic airbreathing propulsion.

Recently, the hypersonic airbreathing propulsion research community has devoted much effort to the study of the supersonic combustion ramjet (scramjet),[10] which is an engine that relies on diffusion-dominated combustion. The oncoming hypersonic airstream temperature and pressure are raised in the inlet as the airstream is decelerated to supersonic speeds by a series of oblique shocks. Fuel is subsequently injected into the combustor, where diffusive mixing and burning occur simultaneously at supersonic speeds. The combustion products are then expanded through a nozzle to provide thrust.

The shock-induced combustion ramjet (shcramjet) concept in hypersonic airbreathing propulsion aims at increasing the performance of conventional scramjet designs by replacing the long scramjet combustor by a much shorter one that employs a very thin detonation wave. This design requires a premixed fuel–air flow to enter the combustor; hence, fuel (hydrogen) injection occurs near the leading edge of the shcramjet.[11] A proper, fundamental understanding of standing ODWs is therefore crucial to future advances in shcramjet technologies.

The typical structure of an oblique detonation wave stabilized over a wedge is shown in Fig. 1. This structure was studied and described in detail by Li et al.[3] and Papalexandris[12] by means of numerical simulations and observed experimentally by Viguier et al.[13] A shock formed by a wedge (which deflects the flow by an angle δ) increases the temperature of the oncoming fuel–air mixture above the ignition point of the fuel. This shock is termed the combustion-inducing shock. In the induction region—the region between the combustion-inducing shock and the first deflagration wave—concentration of radicals increases (with temperature and pressure remaining almost constant) until exothermic reactions begin and deflagration waves are formed. These propagate at the local Mach angle. Each successive deflagration wave has a steeper angle than the previous one due to the temperature rise across each successive wave.[3] The deflagration waves merge, at first, until they intersect with the combustion-inducing shock. The shock and deflagration waves become coupled into a single structure, which is termed an ODW. The ODW angle (ε) is steeper than the combustion-inducing shock angle. A slip line (contact surface) is also formed, which separates the component of flow passing through the ODW and the component of flow passing through the shock and the deflagration waves. This latter component is also termed the shock-induced combustion zone.

A limiting condition for detonation waves is the Chapman–Jouguet (CJ) point of minimum entropy where the Mach number of the combustion products downstream of the wave is unity; this implies a self-sustaining detonation. For the case of ODWs, the CJ condition corresponds to a particular wedge angle, δ_{CJ}, which gives rise to a CJ ODW at an angle ε_{CJ}; the normal component of the Mach number downstream of this ODW is unity. It has been observed, in a series of both inviscid[14] and viscous[15] numerical simulations, that lowering the wedge angle below δ_{CJ} does not entail a lower ODW angle than ε_{CJ}; this reinforces the notion of a self-sustaining detonation at the CJ point. Because the CJ point also corresponds to minimum entropy production, the shcramjet is usually designed to operate with an ODW close to CJ conditions.[11]

For certain levels of overdrive (i.e., at a high enough wedge angle), Powers et al.[16,17] have predicted that oblique detonations cannot stabilize over a wedge. Their numerical studies were based on the two-dimensional Euler equations for a calorically perfect gas with an irreversible one-step exothermic chemical reaction governed by Arrhenius kinetics. Li et al.[3] also predicted, with a more detailed combustion model, that removing the nitrogen component of air for ODWs at a certain level of overdrive can lead to an unstable detonation. Other researchers[12,18–20] have numerically predicted, with chemical models of varying complexity, that ODWs can be stabilized over a wedge. Thaker and Chelliah[21] have demonstrated numerically how to reduce the complexity of the chemical models to achieve an ODW solution. Furthermore, in a 1995 experiment, Morris et al.[22] were able to show evidence of a detonation wave stabilized over a wedge. Numerical analyses by Choi et al.,[23] however, claim that the experiment run time was too short to capture what was supposed to be an oscillatory behavior in the detonation structure.

In light of this uncertainty in ODW stability, it is vital for shcramjet propulsion research to determine whether a detonation wave near CJ conditions can be stabilized over a wedge from flow conditions typical of a shcramjet combustor inlet (i.e., a Mach number of ~7, pressure of ~23 kPa, and a temperature of ~750 K). Furthermore, it is crucial to determine whether the said ODW is resilient to inhomogeneities in the oncoming fuel–air mixture because it is expected that the mixing in the inlet will not produce a perfectly homogeneous, stoichiometric fuel–air mixture. Li et al.[3] conducted a numerical simulation where a large disturbance composed of a region

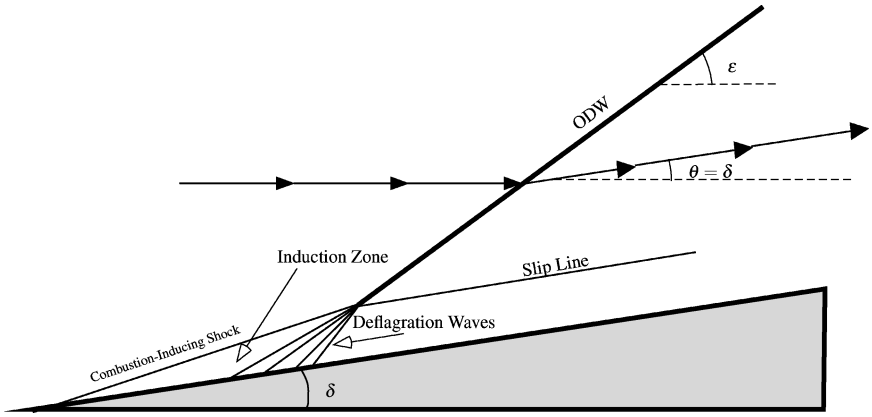

Fig. 1 Schematic of an ODW (θ is the flow angle).

of intermediate radicals was introduced into a flowfield containing an ODW and showed that the detonation structure was very resilient to this disturbance. This is a very promising result that needs to be confirmed with disturbances that simulate incomplete mixing of fuel and air.

Many of the aforementioned studies investigating ODWs are inviscid in nature; however, Li et al.[24] and Fusina[15] carried out numerical simulations investigating the effects of boundary layers on ODWs and concluded that the overall detonation structure is very similar in viscous and inviscid flow.

This study addresses two main issues concerning the use of standing ODWs for the purposes of shcramjet propulsion. First, the issue of stabilizing an ODW at CJ conditions over a wedge will be studied. In essence, the formation of a detonation wave from a premixed hydrogen–air flow impinging on a wedge will be time-accurately simulated. Second, the detonation wave's stability in the presence of inhomogeneities in the oncoming fuel–air mixture will be tested by other time-accurate simulations. The induction process and radical formation in the shock-induced combustion zone of the ODW structure will also be analyzed. Finally, note that hydrogen is the choice of fuel used in the present simulations.

Physical Model and Numerical Method

The laminar, two-dimensional, multispecies Navier–Stokes equations are used herein to model the physical system. They are written as follows in tensor form in curvilinear coordinates[25–27]:

$$\frac{\partial}{\partial t}\boldsymbol{Q}+\sum_{i=1}^{n_d}\left[\frac{\partial F_i}{\partial X_i}-\sum_{j=1}^{n_d}\frac{\partial}{\partial X_i}\left(K_{ij}\frac{\partial G}{\partial X_j}\right)\right]=S \tag{1}$$

where the vector of conservative variables, $\boldsymbol{Q}$, convection fluxes F_i, diffusion fluxes G, and source terms S can each be written as[27]

$$Q=\frac{1}{J}\begin{bmatrix}\rho Y_1\\ \vdots\\ \rho Y_{n_s}\\ \rho v_1\\ \vdots\\ \rho v_{n_d}\\ \rho E\end{bmatrix},\qquad F_i=\frac{1}{J}\begin{bmatrix}\rho V_i Y_1\\ \vdots\\ \rho V_i Y_{n_s}\\ \rho V_i v_1+X_{i,1}P\\ \vdots\\ \rho V_i v_{n_d}+X_{i,n_d}P\\ \rho V_i E+V_i P\end{bmatrix}$$

$$G=\begin{bmatrix}Y_1\\ \vdots\\ Y_{n_s}\\ v_1\\ \vdots\\ v_{n_d}\\ T\end{bmatrix},\qquad S=\frac{1}{J}\begin{bmatrix}\dot{W}_1\\ \vdots\\ \dot{W}_{n_s}\\ 0\\ \vdots\\ 0\\ 0\end{bmatrix} \tag{2}$$

The diffusion matrix K_{ij} is given by[27]

$$K_{ij}=\begin{bmatrix}\alpha_{i,j}\mathcal{D}_1 & \cdots & 0 & 0 & \cdots & 0 & 0\\ \vdots & \ddots & \vdots & \vdots & \ddots & \vdots & \vdots\\ 0 & \cdots & \alpha_{i,j}\mathcal{D}_{n_s} & 0 & \cdots & 0 & 0\\ 0 & \cdots & 0 & \mu\beta_{i,j}^{1,1} & \cdots & \mu\beta_{i,j}^{1,n_d} & 0\\ 0 & \cdots & 0 & \vdots & \ddots & \vdots & 0\\ 0 & \cdots & 0 & \mu\beta_{i,j}^{n_d,1} & \cdots & \mu\beta_{i,j}^{n_d,n_d} & 0\\ \alpha_{i,j}h_1\mathcal{D}_1 & \cdots & \alpha_{i,j}h_{n_s}\mathcal{D}_{n_s} & \mu\sum_m v_m\beta_{i,j}^{m,1} & \cdots & \mu\sum_m v_m\beta_{i,j}^{m,n_d} & \alpha_{i,j}\kappa\end{bmatrix} \tag{3}$$

where α and β correspond to

$$\alpha_{i,j}=\frac{1}{J}\sum_{m=1}^{n_d}X_{j,m}X_{i,m}$$

$$\beta_{i,j}^{mn}=\alpha_{i,j}\delta_{mn}^{K}+\frac{1}{J}X_{j,m}X_{i,n}-\frac{2}{3}\frac{1}{J}X_{j,n}X_{i,m} \tag{4}$$

The rate of change of the distance in the curvilinear coordinate system with respect to the Cartesian coordinate system, $X_{i,j}$, is given by

$$X_{i,j}=J\left[\left(2\delta_{i,j}^{K}-1\right)\frac{\partial x_{j+1}}{\partial X_{i+1}}\right] \tag{5}$$

in two dimensions. The inverse of the metric Jacobian, $1/J$, also in two dimensions, corresponds to

$$\frac{1}{J}=\frac{\partial x_1}{\partial X_1}\frac{\partial x_2}{\partial X_2}-\frac{\partial x_1}{\partial X_2}\frac{\partial x_2}{\partial X_1} \tag{6}$$

The contravariant velocity V_i has the usual definition:

$$V_i\equiv\sum_{j=1}^{n_d}X_{i,j}v_j \tag{7}$$

Note that v_i is the velocity component of the mixture in the x_i direction; Y_k is the mass fraction of species k; h_k is the enthalpy of species k; T, P, and ρ are the mixture temperature, pressure, and density, respectively; δ_{ij}^{K} is the Kronecker delta; n_d is the number of dimensions; and n_s is the number of species. The total energy of the mixture, E, is given by

$$E=e+\sum_{j=1}^{n_d}\frac{v_j^2}{2} \tag{8}$$

The Navier–Stokes equations are closed by the thermal and caloric equations of state:

$$P=\sum_{k=1}^{n_s}\rho Y_k R_k T \tag{9}$$

$$e=\sum_{k=1}^{n_s}Y_k h_k-\frac{P}{\rho} \tag{10}$$

where R_k is the gas constant for species k and the species enthalpies are calculated from

$$h_k=R_k\left(a_{1,k}T+\frac{a_{2,k}}{2}T^2+\frac{a_{3,k}}{3}T^3+\frac{a_{4,k}}{4}T^4+\frac{a_{5,k}}{5}T^5+a_{6,k}\right) \tag{11}$$

where the coefficients $a_{1,k}$ to $a_{6,k}$ are part of McBride's polynomial formulation[28] of the thermochemical data found in the JANAF tables.[29] These polynomials can also be used to calculate the species-specific heats at constant pressure, c_{Pk}:

$$c_{Pk}=R_k\left(a_{1,k}+a_{2,k}T+a_{3,k}T^2+a_{4,k}T^3+a_{5,k}T^4\right) \tag{12}$$

The McBride polynomials are valid from a temperature of 200 to 6000 K.

The mixture viscosity μ, mixture thermal conductivity κ, and species mass diffusion coefficient $\mathcal{D}_k$ are determined from the kinetic theory of gases[30] for a derivation of the needed expressions). The formulation of mass diffusion within Eqs. (1–3) implies the use of Fick's law in the mass conservation equation. Pressure and thermal diffusion effects are not included, but the energy transfer due to a concentration gradient is modeled in the energy equation [see the last row of the diffusion matrix in Eq. (3)]. The rates of species production due to nonequilibrium chemical reactions, $\dot{W}_k$, are determined from Arrhenius chemical kinetics.[31] Each species production term (in kilograms per second) is given by

$$\dot{W}_k = m_k \sum_{l=1}^{N_e} (\nu''_{l,k} - \nu'_{l,k}) \left(k_{f,l} \prod_{m=1}^{N_l} [\chi_m]^{\nu'_{l,m}} - k_{b,l} \prod_{m=1}^{N_l} [\chi_m]^{\nu''_{l,m}} \right) \tag{13}$$

where N_e is the number of elementary reactions involving species k, N_l is the number of species involved in the elementary reaction, m_k is the molecular weight of species k, χ_m is the mole fraction of species m, $\nu'_{l,k}$ is the stoichiometric coefficient for the reactants of reaction l, $\nu''_{l,k}$ is the stoichiometric coefficient for the products of reaction l, k_b is the backward reaction rate constant, and k_f is the forward reaction rate constant, given by the modified Arrhenius equation

$$k_f = \mathcal{A} T^n \exp(-\mathcal{E}/\mathcal{R}T) \tag{14}$$

The coefficients $\mathcal{A}$, n, and $\mathcal{E}$ for each elementary reaction are tabulated in so-called combustion models. Here, a reduced form of the model developed by Lutz et al.[32] was used for hydrogen–air combustion. It employs 20 reactions and 9 species with nitrogen inert and it is shown in Table 1. This model is henceforth referred to as the Lutz model.

The backward and forward reaction rate constants are related by the equilibrium constant K_c:

$$K_c = k_f / k_b \tag{15}$$

The equilibrium constant K_c is given by

$$K_c = (\mathcal{R}T)^{-\Delta\nu} \exp(-\Delta G^o / \mathcal{R}T) \tag{16}$$

where

$$\Delta\nu = \sum_{i=1}^{N_l} (\nu''_i - \nu'_i) \tag{17}$$

Table 1 Lutz combustion model equations and parameters[a]

Reaction	A	n	E
(1) $H_2 + O_2 \rightleftharpoons OH + OH$	1.70×10^{13}	0	47,780
(2) $OH + H_2 \rightleftharpoons H_2O + H$	1.17×10^{09}	1.3	3,626
(3) $O + OH \rightleftharpoons O_2 + H$	4.00×10^{14}	−0.5	0
(4) $O + H_2 \rightleftharpoons OH + H$	5.06×10^{04}	2.67	6,290
(5) $H + O_2 + M \rightleftharpoons HO_2 + M$	3.61×10^{17}	−0.72	0
(6) $OH + HO_2 \rightleftharpoons H_2O + O_2$	7.50×10^{12}	0	0
(7) $H + HO_2 \rightleftharpoons OH + OH$	1.40×10^{14}	0	1,073
(8) $O + HO_2 \rightleftharpoons O_2 + OH$	1.40×10^{13}	0	1,073
(9) $OH + OH \rightleftharpoons O + H_2O$	6.00×10^{08}	1.3	0
(10) $H + H + M \rightleftharpoons H_2 + M$	1.00×10^{18}	−1.0	0
(11) $H + H + H_2 \rightleftharpoons H_2 + H_2$	9.20×10^{16}	−0.6	0
(12) $H + H + H_2O \rightleftharpoons H_2 + H_2O$	6.00×10^{19}	−1.25	0
(13) $H + OH + M \rightleftharpoons H_2O + M$	1.60×10^{22}	−2.0	0
(14) $H + O + M \rightleftharpoons OH + M$	6.20×10^{16}	−0.6	0
(15) $O + O + M \rightleftharpoons O_2 + M$	1.89×10^{13}	0	−1,788
(16) $H + HO_2 \rightleftharpoons H_2 + O_2$	1.25×10^{13}	0	0
(17) $HO_2 + HO_2 \rightleftharpoons H_2O_2 + O_2$	2.00×10^{12}	0	0
(18) $H_2O_2 + M \rightleftharpoons OH + OH + M$	1.30×10^{17}	0	45,500
(19) $H_2O_2 + H \rightleftharpoons HO_2 + H_2$	1.60×10^{12}	0	3,800
(20) $H_2O_2 + OH \rightleftharpoons H_2O + HO_2$	1.00×10^{13}	0	1,800

[a]The units for A are in [$\mathrm{cm}^{3b}/(\mathrm{gmol} - \mathrm{s})^b$], where $b = 1$ for two-body reactions and $b = 2$ for three-body reactions; E is in [cal/gmol].

Table 2 Third-body efficiencies for Lutz combustion model

	Third-body efficiency		
Reaction	H_2	H_2O	N_2
(5) $H + O_2 + M \rightleftharpoons HO_2 + M$	1.86	18.6	1.26
(13) $H + OH + M \rightleftharpoons H_2O + M$	1.0	5.0	1.0
(14) $H + O + M \rightleftharpoons OH + M$	1.0	5.0	1.0

and ΔG^o is the difference in Gibbs free energy between products and reactants in a particular reaction, calculated at a reference pressure of 1 atm, given by

$$\Delta G^o = \sum_{k=1}^{N_l} (\nu''_k - \nu'_k)\left(\hat{h}_k - T s^o_k\right) \tag{18}$$

where $\hat{h}_k$ is the molar enthalpy of species k, and s^o_k is the molar entropy of species k calculated at a reference pressure of 1 atm. Finally, note that in Table 1 the symbol M denotes a third-body collision partner, a species acting as a catalyst only. The molar concentration, M, is simply determined from the following equation:

$$\chi_M = \sum_{k=1}^{n_s} \eta_k \chi_k \tag{19}$$

where η_k is the third-body efficiency; η_k is unity for most species and reactions except those listed in Table 2. The computational results were obtained with the window allocatable resolver for propulsion (WARP) computational fluid dynamics (CFD) code.[27,33] It employs a total variational diminishing Yee–Roe scheme[18,34] for convective flux discretization, central differences for diffusive flux discretization, and a block-implicit approximate factorization algorithm to advance the solution in pseudotime. For time-accurate simulations, time accuracy is regained by a dual time-stepping method.[35] To achieve faster convergence, WARP uses a domain decomposition technique termed the marching window cycle; it is important to note that it does not modify the discretized residual, the block-implicit factorization scheme, the dual time-stepping scheme, or the convergence criterion.[27,33]

In WARP, the residual of the laminar Navier–Stokes equations is defined in tensor form in curvilinear coordinates as[27]:

$$R = \sum_{i=1}^{n_d} \left[\frac{\partial F_i}{\partial X_i} - \sum_{j=1}^{n_d} \frac{\partial}{\partial X_i} \left(K_{ij} \frac{\partial G}{\partial X_j} \right) \right] - S \tag{20}$$

and convergence is attained when

$$\xi \le \xi_{\text{verge}} \tag{21}$$

for all inner nodes, where ξ is a convergence criterion based on the maximum between the discretized continuity and energy residuals[27]:

$$\xi \equiv \max\left(\frac{\left| R_\Delta^{\text{continuity}} \right|}{J^{-1}\rho}, \frac{\left| R_\Delta^{\text{energy}} \right|}{J^{-1}\rho E} \right) \tag{22}$$

The user-defined convergence threshold ξ_{verge} is set to a value at least four orders of magnitude smaller than the initial value of ξ for all the numerical simulations mentioned herein.

The WARP code has been validated with experimental results from Holden and Moselle,[36] Morris et al.,[22] and Lehr[6] that feature shock–boundary layer interactions, shock-induced combustion, and detonation phenomena, respectively. For a detailed explanation of these validation cases, see Ref. 15. WARP was shown to be capable of reproducing these experimental results with a sufficient degree of accuracy provided the spatial resolution was adequate. For example, in Lehr's blunt-body experiments where a projectile was fired into a quiescent hydrogen–air mixture at a subdetonative speed, a simulation with WARP was able to reproduce the resulting frequency

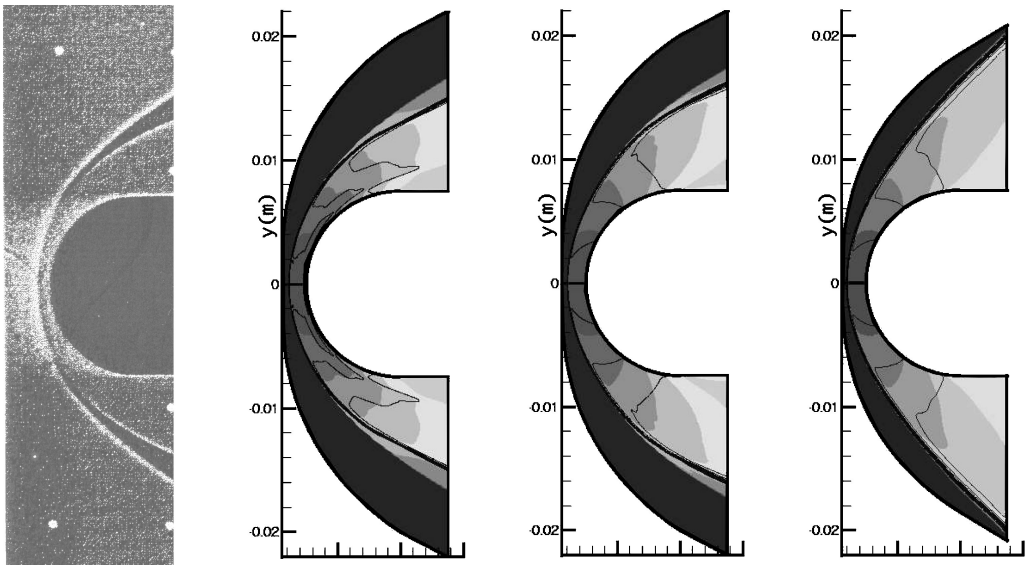

Fig. 2 Shadowgraph (left panel) of Lehr's blunt-body experiment for the superdetonative case overlaid temperature contours (flood: 15 levels between 450 and 3400 K) and water contours (lines: 15 levels between 0.01 and 0.21) from numerical results from WARP using three different grid resolutions: 400 × 600, 200 × 300, and 60 × 90 (right panels).

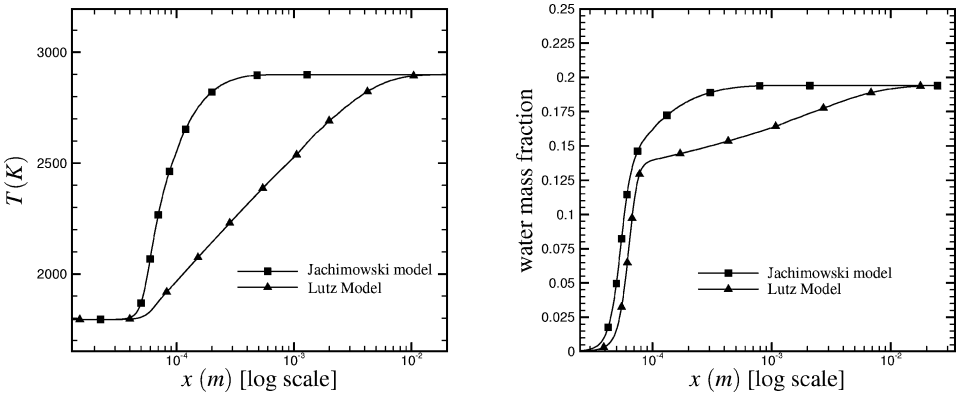

Fig. 3 Comparison of the spatial variation of temperature (left) and water mass fraction (right) within the one-dimensional ODW by using the two different combustion models; in this case the ODW angle is 24.875 deg.

of the oscillating shock-combustion front to within 6%; and, for the steady case where the projectile is fired at a superdetonative speed, the position of the combustion front at the trailing edge of the projectile was captured to within 2% with the finest grid used (Fig. 2).

Results and Discussion

Finding the Chapman–Jouguet Point

The initial inflow conditions used here were as follows: a stoichiometric hydrogen–air mixture at a Mach number of 7, a temperature of 750 K, and a pressure of 23 kPa. These conditions correspond approximately to those at a shcramjet's combustor inlet.[11] For these conditions, the CJ point was determined by using two separate methods: an iterative procedure solving the one-dimensional Rankine–Hugoniot equations coupled with species conservation equations (together with the Lutz combustion model) to find the species production terms, and a series of two-dimensional steady-state simulations with WARP (using laminar flow and a fixed-temperature wall boundary condition at 750 K). In the one-dimensional case, a value of ε is specified a priori, and the spatial variation of flow properties along the ODW is found by solving the Rankine–Hugoniot equations and the species conservation equations. The post-ODW velocity and ε are then used to calculate δ.

Regarding the validity and choice of the Lutz combustion model, in shock-induced combustion simulations, usually the Jachimowski[37] combustion model is used,[7,11,23] which has been well validated.[7,11,15] The physical reason for choosing the Lutz model stems from the fact that it was developed for inhomogeneous reacting gas mixtures analogous to the ones that will be present in the subsequent ODW stability simulations.

One test of validity of the Lutz model was conducted by comparing the one-dimensional solutions described earlier to similar solutions using the Jachimowski model. In all cases, the post-ODW properties of both models were identical. This gives at least some validity to the Lutz model. However, the Lutz model gave rise to a thicker reaction zone within the ODW: this length was 1 cm, whereas for Jachimowski model it was 1 mm. These results are exemplified in Fig. 3.

Experimental data from Strauss and Scott[38] were also used to test the Lutz model. Strauss and Scott observed the speed and postdetonation pressure of several detonation waves arising from a stoichiometric hydrogen–oxygen mixture at various initial pressures, with the initial temperatures always fixed at 300 K. The experiments were simulated numerically by solving the Rankine–Hugoniot equations coupled with the Lutz combustion model as before. Because the numerical solution is in the detonation-wave frame of reference, the postdetonation pressure was used for comparison. Two cases were compared: one where the initial pressure was 1 atm and one where it was 5 atm. In both cases, the numerical solution and experimental values of the postdetonation pressure were within 5% of each other.

One further reason to use the Lutz model came from grid requirements. The computational grid for the two-dimensional simulations was chosen to be constructed such that approximately 20 points

could be placed in the reaction zone of the ODW and such that the resolution could be uniform outside the boundary layer. Had the Jachimowski model been used, a 1-mm ODW thickness would have led to a very small grid resolution and an intractable grid size for the CPU resources available. It is true that, by using the Jachimowski model, a smaller computational domain could have been employed, thus reducing the total grid size; however, this smaller computational domain still would have been too large for the small resolution that a "Jachimowski ODW" would have required due to the length of the shock-induced combustion zone. An artificial detonation thickening procedure was therefore employed by means of the Lutz model to obtain a more tractable grid size for the CPU resources available.

In the two-dimensional WARP simulations, δ is set initially and ε is measured from the resulting flowfield. Tables 3 and 4 summarize the results of both the one- and two-dimensional approaches. It was not possible to obtain an underdriven ODW solution using the one-dimensional Rankine–Hugoniot equations coupled with the Lutz combustion model; hence, the CJ point was inferred to be at the value of the lowest ε (and subsequent resulting δ) that yielded a solution to the Rankine–Hugoniot equations. For the two-dimensional WARP simulations, the CJ point is inferred at the particular value of δ whereby a further decrease in δ did not result in a decrease in ε. From the two sets of results, the CJ point was therefore inferred to correspond to a value of δ between 10 and 10.5 deg.

Table 3 Summary of results for one-dimensional ODW model

δ, deg	ε, deg
15.7	27.000
13.9	26.000
11.2	25.000
10.6	24.900
10.3	24.875

Grid Convergence Study

The computational domain for the ODW formation and stability simulations is such that the wedge surface is horizontal and the flow impinges on the wedge surface at an angle δ. The flow deflection angle chosen was 10.5 deg, which, according to the analyses in the preceding section, leads to the formation of an ODW just above the CJ point. The size of the computational domain was 0.6 m by 0.13 m.

The grid resolution was chosen to be uniform in the computational domain (except in the boundary layer) and was constructed such that approximately 20 grid points could be placed within the reaction zone of the ODW. Fifty grid points were placed in the boundary-layer region, which was roughly estimated to be 3 mm thick.

Thus, the grid was constructed to contain 400 points in the x direction and 300 points in the y direction. The domain and inflow conditions used are as those shown in Fig. 4. The fully formed flowfield can be seen in Fig. 4, as well as in Fig. 5.

The spatial accuracy of the (400×300) grid was assessed by a grid convergence study carried out with steady-state simulations of the formation of the near-CJ ODW from the conditions described earlier. The results from this grid were compared to results from three other grid levels: 200×150, 800×600, and 1600×1200. The

Table 4 Summary of results for steady-state ODW simulations

ε, deg	δ, deg
23.5	7.5
23.5	8.5
23.5	9.0
23.5	9.5
23.5	10
23.8	10.5
25.0	11
27	16

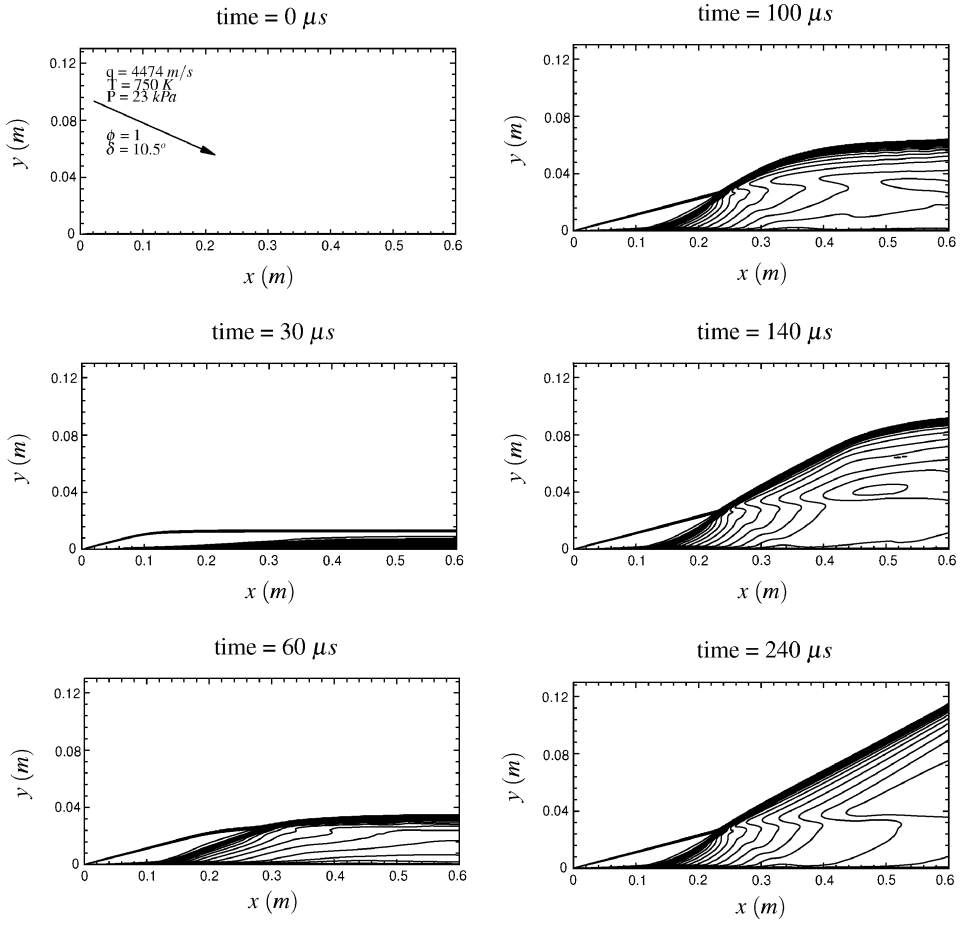

Fig. 4 Temperature contours showing the formation of the ODW; 35 contour levels are used between 700 and 3500 K.

200×100 grid was constructed to contain approximately 10 points within the fully formed ODW; the 800×600 grid, 40; and the 1600×1200 grid, 80. As mentioned previously, the 400×300 grid was constructed with 20 points within the reaction zone of the ODW. In the boundary layer, the 200×150 grid contained 25 grid points; the 400×300, 50; the 800×600, 100; and the 1600×1200, 200.

For the numerical simulations described here, one would expect that, when the grid size is doubled in each direction, there would be a reduction in global error by approximately a factor of two. This is because the Yee–Roe scheme is first-order accurate through discontinuities,[18] and the present flowfields are dominated by discontinuities.

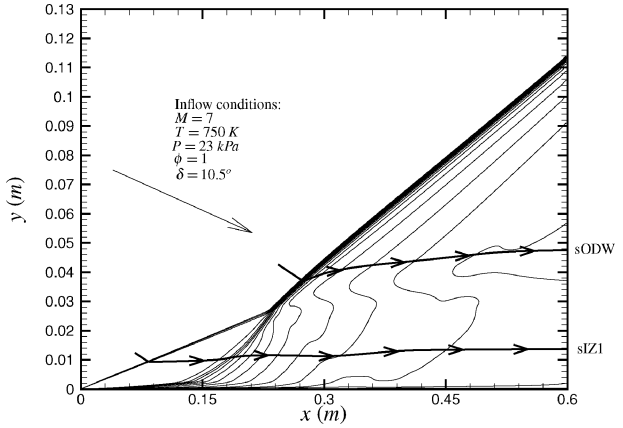

Fig. 5 Location of extracted streamlines with temperature field of the fully formed ODW resulting from a time-accurate simulation run with a 1-μs time step (15 contour levels between 750 and 3000 K are shown).

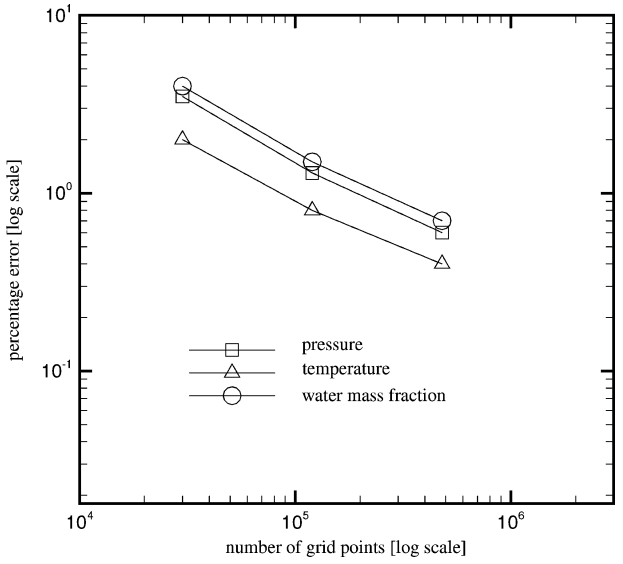

Fig. 6 Error vs grid size plots for integral measures of pressure, temperature, and water mass fraction.

A measure of global error was calculated by integrating pressure, temperature, and the water mass fraction over the computational area and computing the percentage error between these integral quantities on the finest (1600×1200) mesh, and the same quantities on the other meshes. The results are plotted in Fig. 6. As the grid size is quadrupled, the percentage error in the integral value of pressure decreases by almost a factor of four; of temperature, by a factor of four; and of water mass fraction, by almost a factor of six. In a global sense, therefore, these results show that the 400×300 grid is adequate and that, as the grid is refined, we seemingly move toward grid convergence.

Using an integral quantity as an error indicator could be misleading: one could have grid convergence in a part of the domain, but not in others. Furthermore, one could have convergence in one variable but not in others. Therefore, the different grid resolutions were compared in the boundary-layer regions and within the reaction zones. Figure 7 shows the boundary-layer temperature profiles at two different sections in the domain. The first section is located at $x = 0.15$ m, in the region where the leading-edge shock and combustion fronts are separate. The second is located at $x = 0.24$ m, where the shock and combustion fronts meet. We can visually determine that, within the boundary-layer regions shown, the grids used exhibit a convergent behavior. At the worst points, the temperature profile on the 400×300 grid differs by about 8% with respect to the finest grid. Boundary-layer profiles in other vertical sections of the domain were examined and were found to exhibit similar trends, with smaller errors farther downstream.

Pressure and water mass fraction profiles along a horizontal section at $y = 0.01$ m are shown in Figs. 8 and 9. The pressure profile does not show grid-convergent behavior between 0.25 and 0.4 m. This corresponds to the equilibration zone in the shock-induced combustion region of the flowfield. The water mass fraction profile shows good grid-convergent behavior.

Better grid convergence in pressure is seen at different horizontal sections: $y = 0.03$ m and $y = 0.076$ m in Figs. 10 and 11. The water mass fraction profiles (shown in Fig. 12) exhibit good grid-convergent behavior as before.

Figure 13 summarizes the pressure error trends in the different horizontal sections. The percentage error in pressure (that is, the error between the finest mesh and the other meshes) at a particular point (the point corresponding to the greatest error value) along each horizontal section was calculated. As can be seen, better grid convergence is achieved along the sections that pass through the fully formed ODW instead of the shock-induced combustion zone. In the region where there is grid-divergent behavior, the error associated with the 400×300 grid is nevertheless at an acceptably low level: approximately 6%.

A very important measure in this study is the value of the ODW angle ε, because a description of the effect of inflow disturbances on

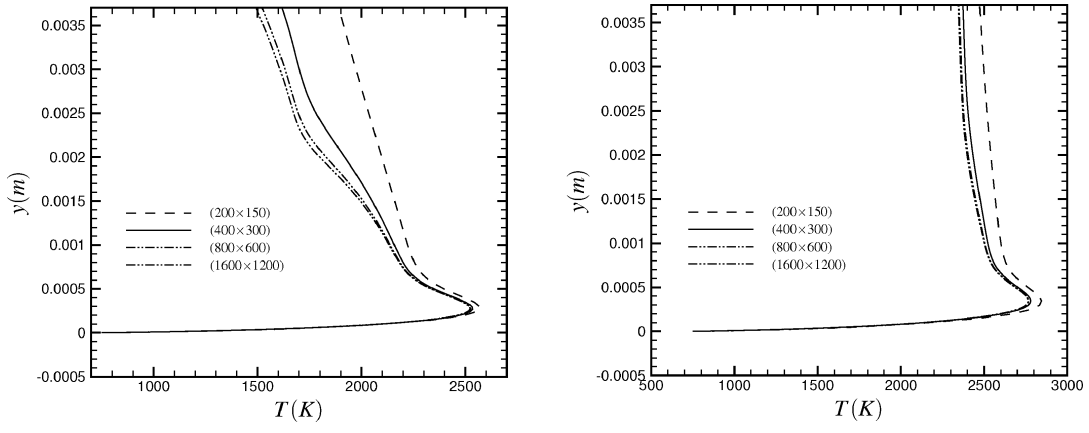

Fig. 7 Boundary-layer temperature profiles at left, $x = 0.15$ m and right, $x = 0.24$ m.

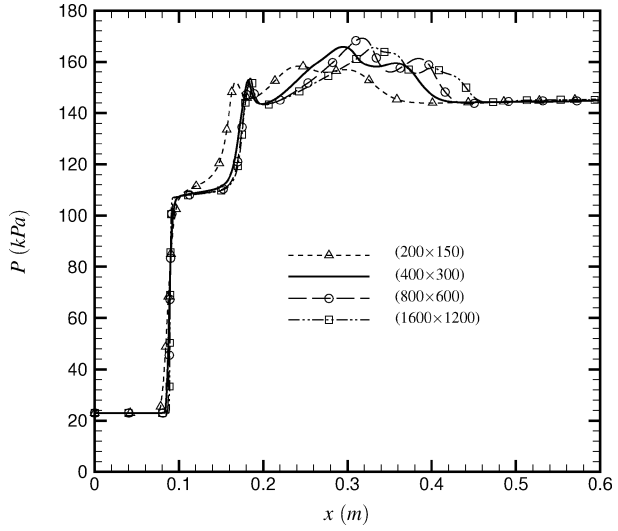

Fig. 8 Horizontal section profiles of pressure at $y = 0.01$ m.

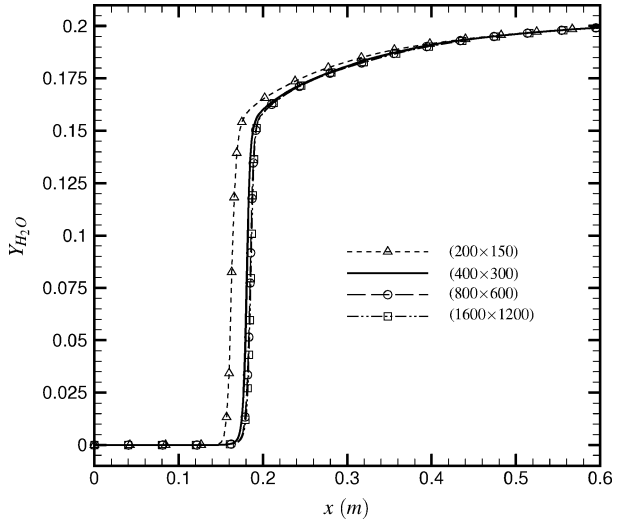

Fig. 9 Horizontal section profiles of water mass fraction at $y = 0.01$ m.

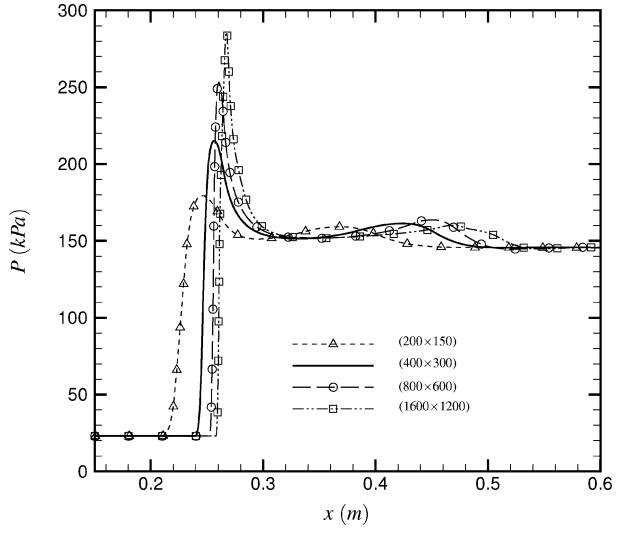

Fig. 10 Horizontal section profiles of pressure at $y = 0.03$ m.

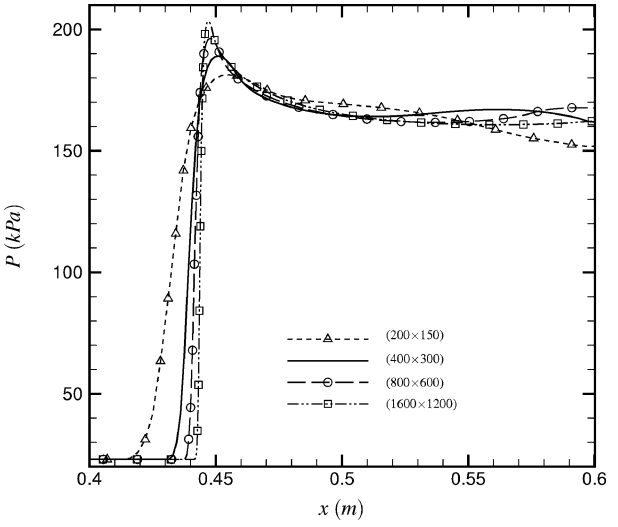

Fig. 11 Horizontal section profiles of pressure at $y = 0.076$ m.

the ODW angle is one of the purposes of this study. This was measured to be 23.8 deg for the 1600×1200 grid. This value differed by less than 1% in all of the other grids.

The preceding analysis seems to indicate a global, generic grid-convergent trend in most regions of the flowfield. The grid resolution chosen for the subsequent simulations, that is, 400×300, is not fine enough to capture all the length scales present, such as the viscous shock thickness, but it is fine enough for determination of "global" or macroscopic phenomena such as the ODW angle, and the possible ODW deflections resulting from inflow disturbances, which are described in a subsequent subsection.

Time-Accurate ODW Formation Simulations

Two different time steps were used for the time-accurate simulation of the formation of the ODW: 1 and 0.1 μs. In both simulations, it was observed that the ODW assumed a stable position after $\sim$240 μs. Figure 4 shows the formation of the ODW by means of temperature fields for the 1-μs-time-step case. The 0.1-μs time step exhibited nearly identical behavior.

The ODW location was tracked throughout the simulation time at the $x = 0.5$ m section for both cases. This was defined to be the y value of the first point along the $x = 0.5$ m section where the water mass fraction was greater than 1%. Figure 14 shows two curves, which represent the two different simulations run with the two different time steps. One can observe the ODW achieving a final, nonoscillatory position. This final position is virtually identical in both cases. The trends in ODW position leading up to the final position are similar, but the values are not identical. Still, the 1-μs time step was deemed sufficient for the subsequent stability simulations, especially in light of the limited available CPU resources.

Induction Process and Radical Formation

Because the combustion model is very detailed, it is possible to analyze the radical formation process in the induction region of the ODW structure. Figure 5 shows two extracted streamlines within the temperature contours of a fully formed ODW resulting from the preceding ODW formation simulation run with a 1-μs time step. Streamline sIZ1 passes through the shock-induced combustion zone, whereas streamline sODW passes through the ODW itself. Figures 15 and 16 show flow properties along streamline sIZ1. It can be seen that between $x = 0.085$ and 0.15 m, the temperature remains constant after the streamline passes through the combustion-inducing shock. This shock causes the temperature and pressure to rise above the ignition point of the hydrogen–air mixture. After the $x = 0.15$ m mark, water concentration and temperature increase rapidly. The $x = 0.15$ m mark can therefore be said to be the start of the energy release period along sIZ1, whereas the section from $x = 0.085$ to 0.15 m can be said to be the induction period. The HO_2 radical is the first to appear in significant amounts in the

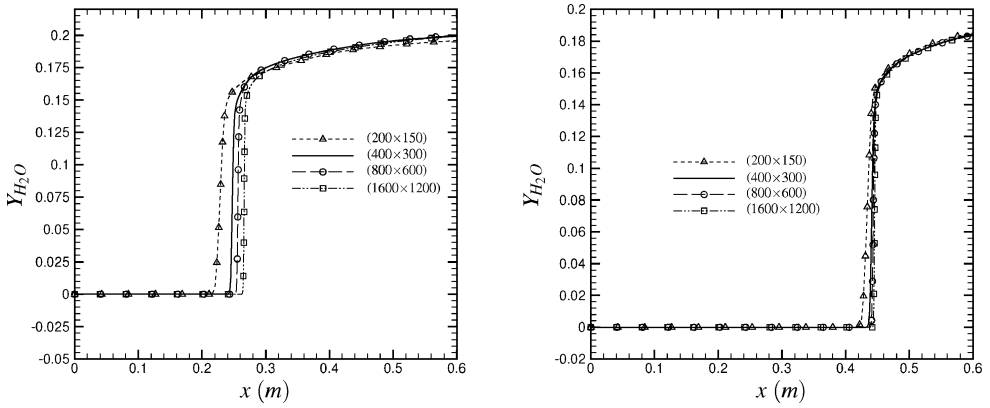

Fig. 12 Horizontal section profiles of water mass fraction at left, $y = 0.03$ m and right, $y = 0.076$ m.

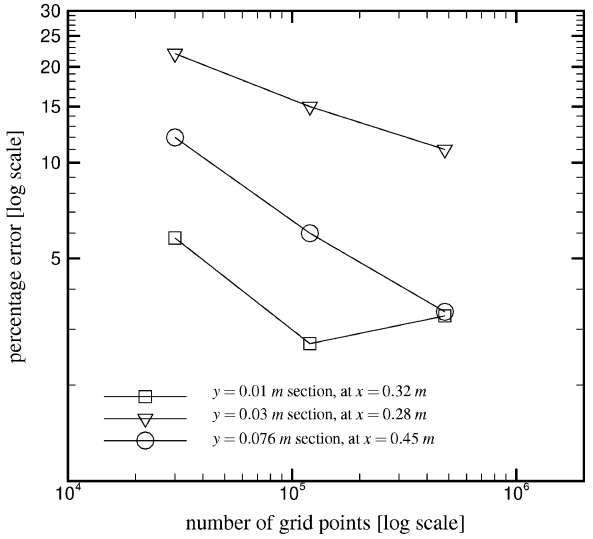

Fig. 13 Error vs grid size plots for local values of pressure along horizontal sections.

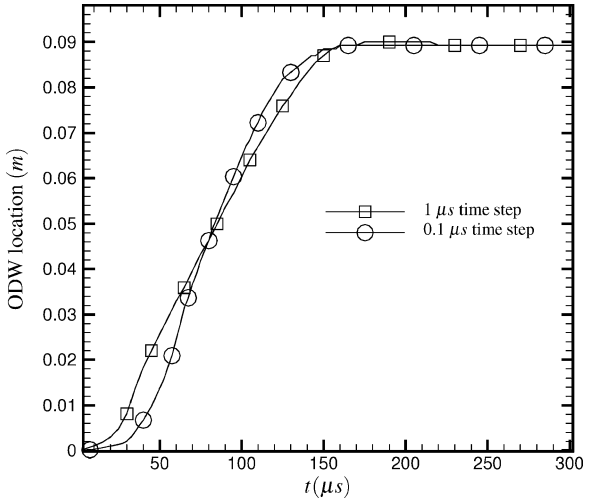

Fig. 14 Location of the ODW at the $x = 0.5$ m section during the simulation time for the two different time steps.

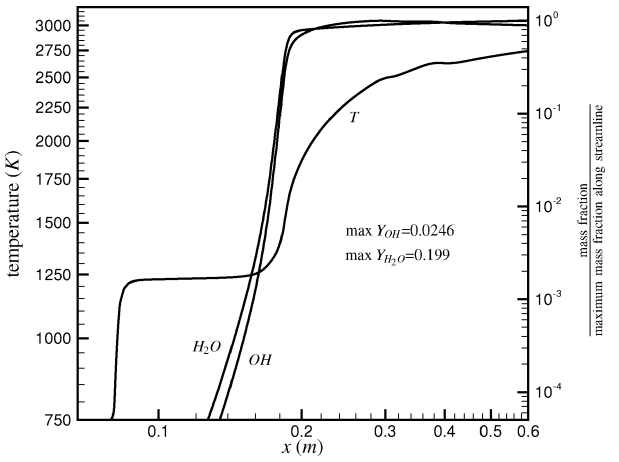

Fig. 15 Log–log plot of temperature, water, and OH mass fraction levels along streamline sIZ1; mass fractions are expressed as a fraction of their maximum values along the streamline.

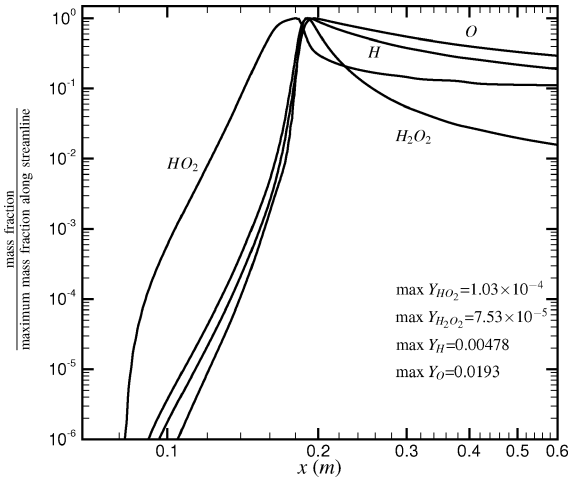

Fig. 16 Log–log plot of HO_2, H_2O_2, H, and O mass fraction levels along streamline sIZ1; mass fractions are expressed as a fraction of their maximum values along the streamline.

induction period; all the other radicals (OH, H, O, and H_2O_2) start to appear close to the $x = 0.15$ m section, that is, close to the start of the energy release period. The sequence at which the species reach 1% of their maximum values along streamline sIZ1 is the following: HO_2 at $x = 0.122$ m, H at $x = 0.164$ m, O at $x = 0.168$ m, H_2O at $x = 0.169$ m, OH at $x = 0.171$ m, and H_2O_2 at $x = 0.171$ m. The sequence at which each of the radicals reaches its maximum value along streamline sIZ1 is HO_2 at $x = 0.181$ m, H_2O_2 at $x = 0.191$ m, H at $x = 0.192$ m, O at $x = 0.196$ m, and OH at $x = 0.196$ m. From these results, it would seem that the HO_2 radical is the key species in the induction region of the ODW, because it is the first to appear and gives rise to the formation of the other radicals and of the combustion product. Reaction (16) in the Lutz model listed in Table 1 is the mechanism for HO_2 formation. From these results, it also appears that OH behaves surprisingly more like a combustion product than an intermediate radical because its concentration does not decay exponentially after reaching its maximum level, as do the

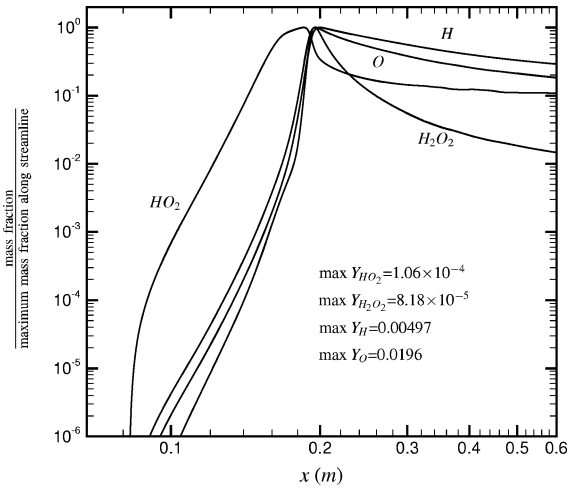

Fig. 17 Log–log plot of HO_2, H_2O_2, H, and O mass fraction levels along streamline sIZ1 extracted from a steady-state ODW formation simulation with the 1600 × 1200 grid; mass fractions are expressed as a fraction of their maximum values along the streamline.

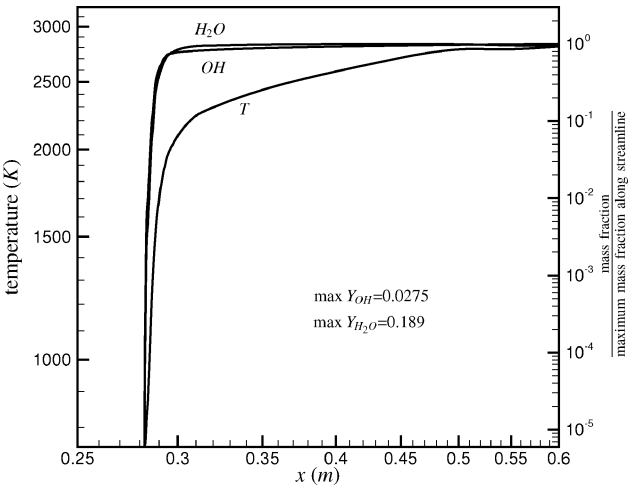

Fig. 18 Log–log plot of temperature, water, and OH mass fraction levels along streamline sODW; mass fractions are expressed as a fraction of their maximum values along the streamline.

concentrations of the other radicals (H, O, HO_2 and H_2O_2); rather, its concentration remains near its maximum value. Reaction (1) in the Lutz model is the main OH-producing reaction. Note the high activation energy for reaction (1) as opposed to the zero activation energy for reaction (16); this explains the early appearance of HO_2 in the induction region as opposed to the late appearance of OH. In the case of shock-induced combustion in an ODW structure, therefore, it is difficult to distinguish between the beginning of the energy release period and the end of the induction period, as evidenced by the close succession of appearance of each species: O, H_2O, and OH appear within 3 mm of each other. The Lutz combustion model's parameters, especially the activation energy, seem to be the dominant factor in the succession of appearance of each species.

It should be pointed out that the grid resolution in the x direction is approximately 1.5 mm, and so there is uncertainty of the accuracy of the sequence of appearance of the species. To reduce this uncertainty, we estimate that the grid should be 10 times finer in the reacting regions. We can, however, compare the trends in radical formation in these results with radical formation trends resulting from a steady-state ODW formation simulation for a grid four times as fine in each direction, used previously in the grid-convergence study section. Figure 17 shows the radical species variation along the same streamline used for Fig. 16, but for a 1600 × 1200 grid. Here, the spatial resolution is approximately 0.375 mm and the trends are very much the same. The radical species succession of appearance along the streamline in the steady-state simulation with the fine grid closely matches (within 3%) those for the time-accurate, coarser 400 × 300 grid case. The only notable difference is the maximum value of H_2O_2, which differs by 8% between the two cases.

Figures 18 and 19 show the temperature and mass fraction levels for streamline sODW, which passes through the ODW itself, again for the ODW resulting from the time-accurate formation simulation with the 400 × 300 grid. Here the most important feature is the near-complete coupling between the induction period and the energy release period. The constant values of temperature in the induction region cannot be observed in these figures due to the induction period being very short. However, a small lag between the temperature rise and the appearance of OH and H_2O can still be observed, whereas increases in HO_2, H, O, and H_2O_2 concentrations occur together with the temperature increase. The HO_2 radical can still be seen as the first to appear in significant concentrations for this streamline. Also note the marked decrease in the maximum value of H_2O as well as the increase in the maximum values of OH, O, and H as compared to streamline sIZ1. The coupling between the combustion-inducing shock and the flame front therefore produces a higher post-ODW temperature, which causes more dissociation.

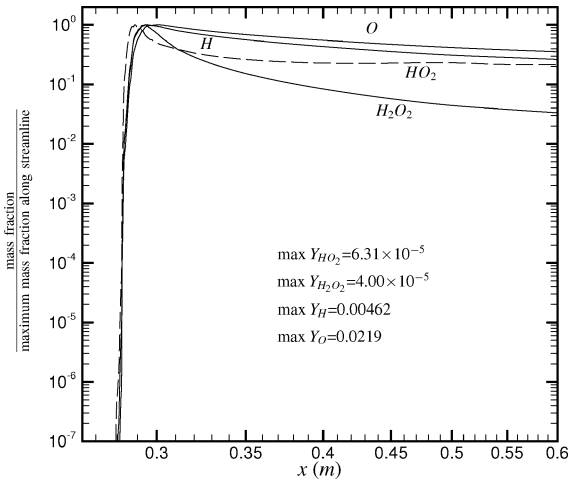

Fig. 19 Log–log plot of HO_2, H_2O_2, H, and O mass fraction levels along streamline sODW; mass fractions are expressed as a fraction of their maximum values along the streamline.

ODW Stability Simulations

As stated previously, the mixing in the inlet of a shcramjet cannot be expected to deliver a perfectly homogeneous, stoichiometric fuel–air mixture at the combustor entrance; hence, study of a (near-) CJ ODW response to inhomogeneities in the oncoming fuel–air mixture was performed. The CJ ODW that was described in the preceding sections was taken as the initial condition for most of the simulations of this section. The nonuniformity of the fuel–air mixture was idealized by a series of "pockets" of fluid, where the equivalence ratio was set to zero and velocity and temperature were set to those of the rest of the mixture. These pockets were artificially placed just upstream of the ODW structure.

Four separate cases were considered, each employing a different pocket size or placement. Each simulation was run with a 1-μs time step and the results of each simulation are summarized in Table 5. The evolution of the density field for two of the cases is shown in Figs. 20–23. Note that, for case 4, an underdriven ODW was considered (formed by a steady-state simulation with $\delta = 8.5$ deg, where the grid resolution was kept the same as in the CJ cases, so that a grid size of 666 × 554 and a domain size of 1 m by 0.24 m was used). The pattern exhibited by the ODW for each stability case shown in these figures is remarkably similar. After the pockets pass through the shock–ODW front, the portion of the ODW near the point where the leading-edge shock and deflagration waves meet moves upstream, and this movement is propagated through the rest

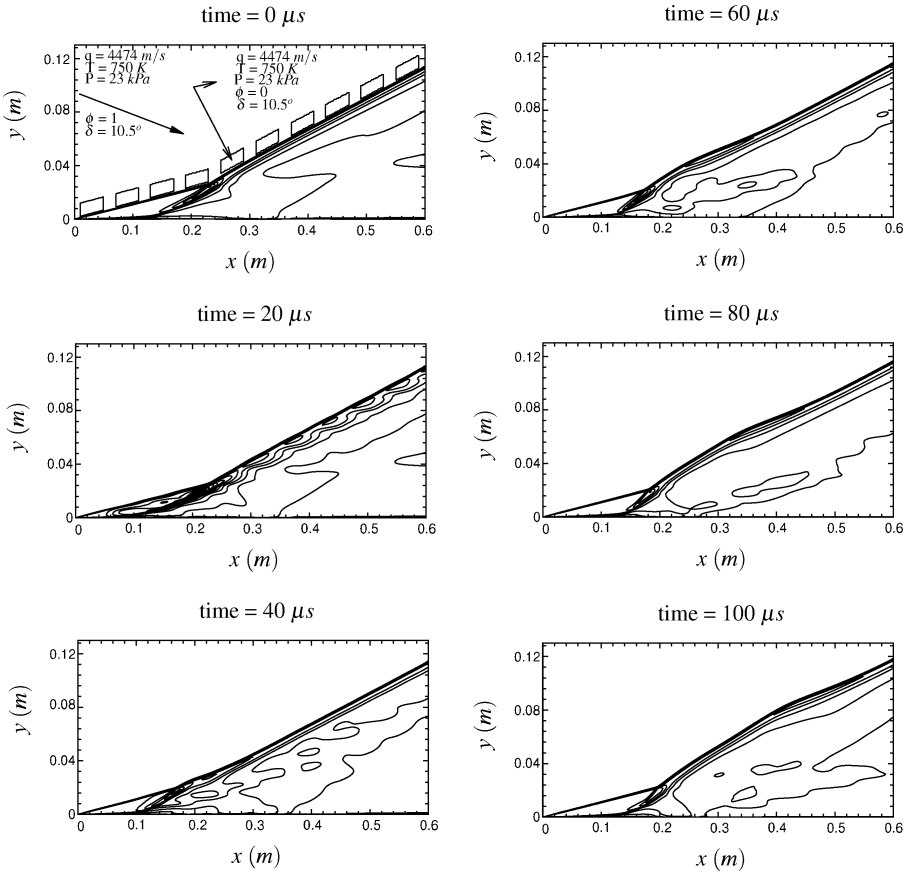

Fig. 20 Density contours showing the displacement of the ODW between 0 and 100 μs due to air pockets placed just upstream of the ODW (case 1 in Table 5); 30 contour levels are used between 0.066 and 0.725 kg/m^3.

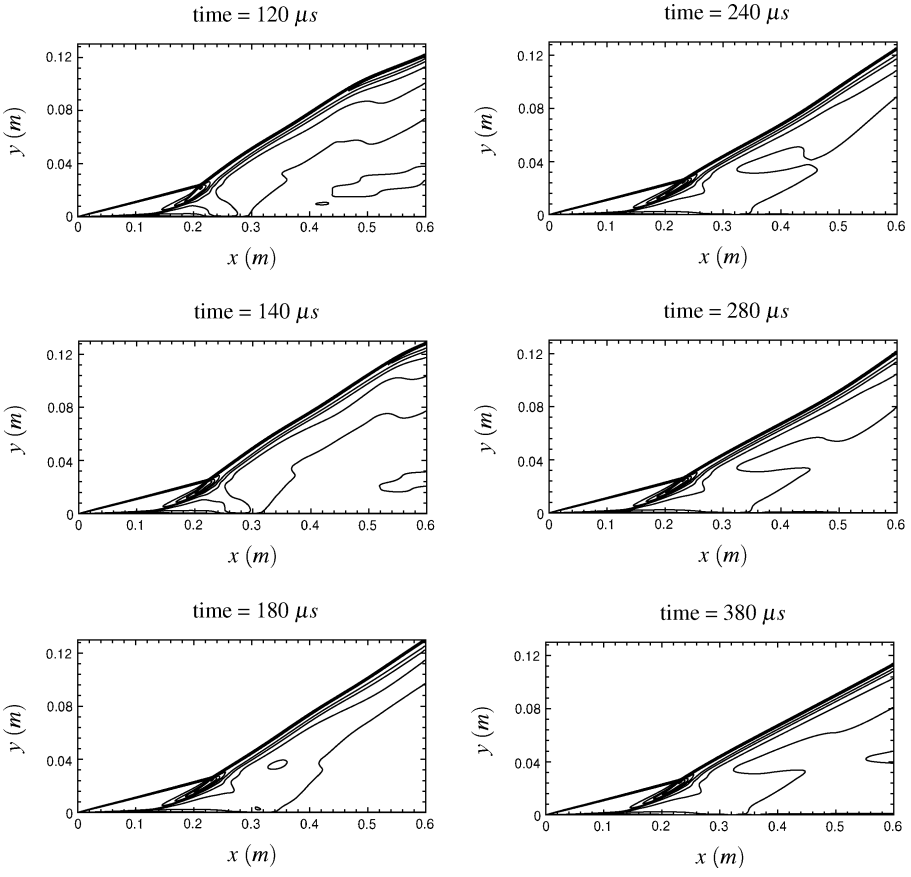

Fig. 21 Density contours showing the displacement of the ODW between 120 and 380 μs due to air pockets placed just upstream of the ODW (case 1 in Table 5); 30 contour levels are used between 0.066 and 0.725 kg/m^3.

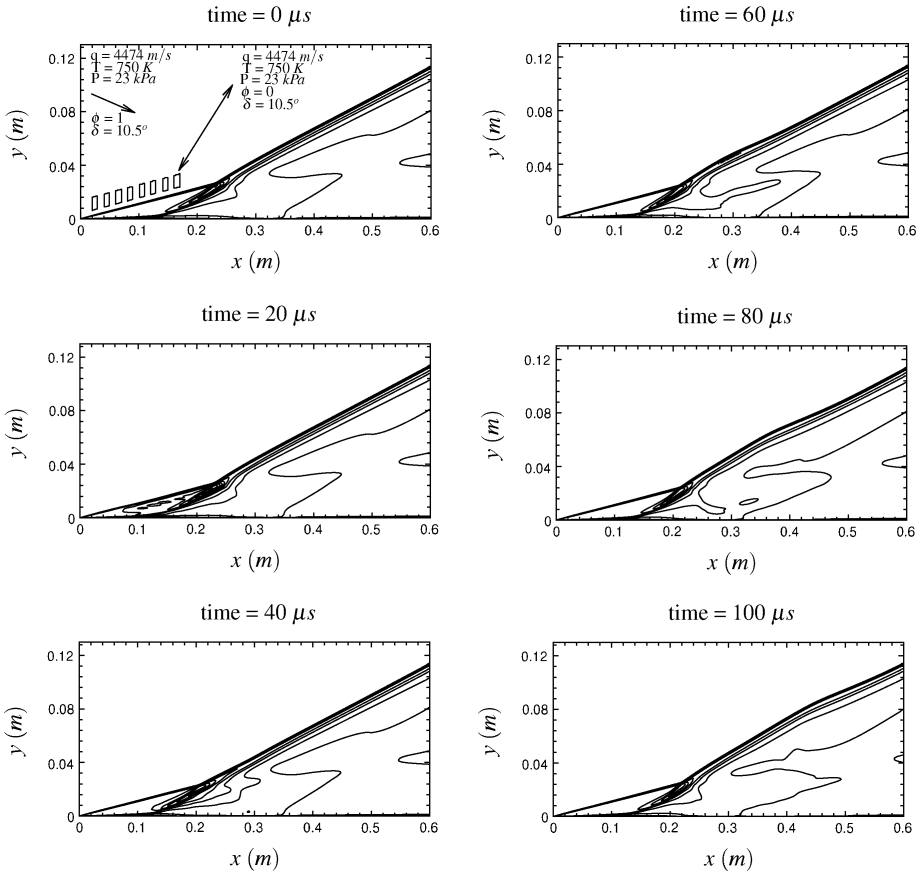

Fig. 22 Density contours showing the displacement of the ODW between 0 and 100 μs due to air pockets placed just upstream of the ODW (case 3 in Table 5); 30 contour levels are used between 0.066 and 0.725 kg/m^3.

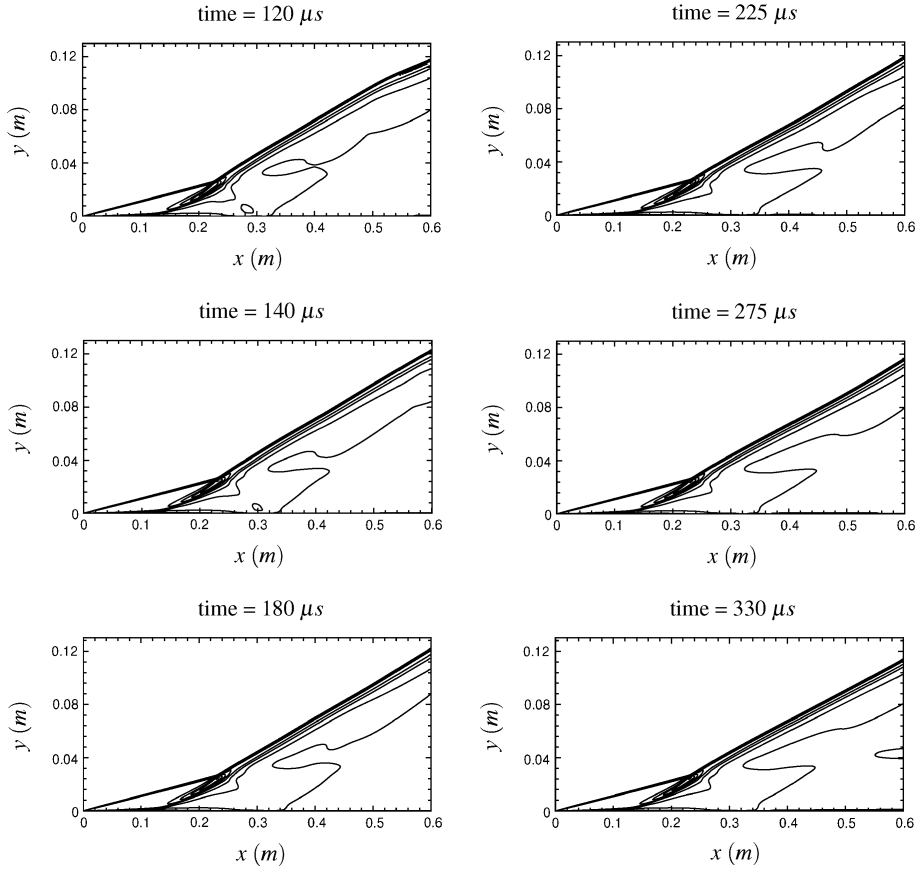

Fig. 23 Density contours showing the displacement of the ODW between 120 and 330 μs due to air pockets placed just upstream of the ODW (case 3 in Table 5); 30 contour levels are used between 0.066 and 0.725 kg/m^3.

Table 5 Summary of stability cases[a]

Case	Air pocket size, mm^2	Air pocket placement, just upstream of	Maximum displacement, mm	Time for return to original position, μs
1	400	LE shock and CJ ODW	15.6	380
2	100	LE shock and CJ ODW	11.8	350
3	100	LE shock only (CJ case)	8.2	330
4	400	LE shock and underdriven ODW ($\delta = 8.5$ deg)	47.8	575

[a]Note that "LE" shock stands for leading-edge shock, which is the combustion inducing shock. The displacement is measured as the vertical displacement of the ODW at the section $x/L = 0.83$ where L is the domain length ($L = 1$ m for the underdriven case and $L = 0.6$ m for the CJ case).

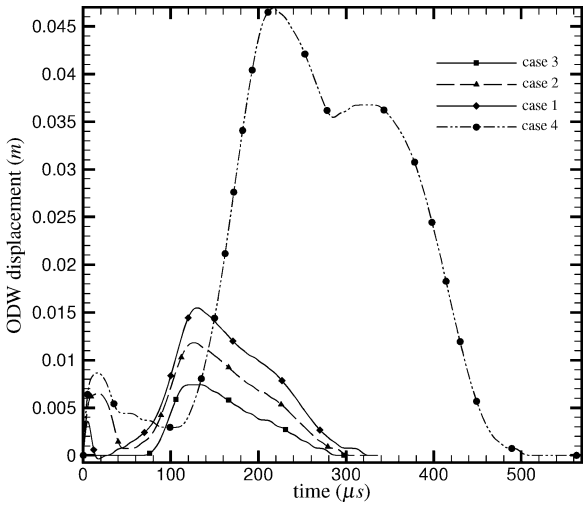

Fig. 24 Variation of ODW displacement through simulation time (graph has been smoothed).

of the ODW until the whole of the ODW has moved to an upstream position. Subsequently, the ODW returns to its original position as the pockets are convected downstream. From these simulations, the ODW structure has been observed to be quite resilient to inhomogeneities in the fuel–air mixture. This was also the case in the ODW stability simulations conducted by Li et al.[3] where an overdriven ODW was perturbed by a single large disturbance made up of intermediate radicals. After displacing upstream, the ODW returned to its original position.

To quantify the displacement of the ODW front, the following strategy was devised. A one-dimensional section was extracted at the 75% mark of the domain in the x direction (i.e., at $x = 0.5$ m for the CJ case and $x = 0.83$ m for the underdriven case) and the temperature profile was tracked along this section through the simulation time. The location of the start of the ODW front can be said to be at the point where the temperature starts to increase. As time advances, this location moves upward (because the ODW is moving upstream as described earlier) until it reaches a maximum and then returns to its original position. Table 5 lists the results of this "displacement quantification" strategy for the different cases. Cases 1–3 show relatively few differences. Case 4, the underdriven case, produced a maximum ODW displacement about three times greater than that of the other cases and the ODW took about one and a half times as long as the near-CJ cases to return to its original position.

Figure 24 tracks the variation of the ODW displacement at the 75% section throughout the simulation time for all cases. One can see that in cases 1, 2, and 4 there is an initial displacement due to the pockets passing through the ODW front. This does not, of course, occur for case 3. After the initial displacement, the ODW reestablishes itself for a short while and then a larger displacement takes place; it reaches a maximum and then the ODW returns to its original position.

The similarity between case 3 and cases 1 and 2 hints at the fact that the passage of the inhomogeneities through the combustion-inducing shock affects the ODW more than their passage through the ODW itself. The presence of the pockets changes the properties of the combustion-inducing shock. A simple one-dimensional oblique shock analysis will show that an oxygen–nitrogen (air) mixture will produce a stronger shock (assuming pressure and velocity are the same) than a stoichiometric hydrogen–air mixture. This is exactly what happens in these ODW stability simulations. The pockets produce a stronger shock: the temperature ratio across this disturbed shock is approximately 2% higher for all the cases and it induces combustion at an earlier position, thus causing the upstream movement of the ODW, which effectively gives the ODW more overdrive. Once the fresh mixture returns, the ODW reestablishes itself to its original position. Although it is true that the pockets produce a stronger shock, it is also true that there is less hydrogen to burn. The pockets of $\phi = 0$ flow diffuse quite rapidly once they have passed through the shock–ODW front; consequently, there is still enough hydrogen present for combustion to take place. Therefore, the increased temperature from the stronger shock offsets the effects of a more fuel-lean mixture.

The displacement of the underdriven ODW is amplified by the larger domain needed to capture the entire structure of the ODW. In particular, the combustion-inducing shock and the induction region are much longer than in a CJ ODW. Disturbing such a combustion-inducing shock affected the underdriven ODW structure in a more severe fashion, as shown in Fig. 24.

Conclusions

The formation and stability of a near-CJ ODW were studied in this paper using time-accurate CFD simulations. Simulating the formation of a near-CJ ODW with 1- and 0.1-μs time steps indicated that it reaches a nonoscillatory position. The CJ ODW was observed to be quite resilient to inhomogeneities in the oncoming fuel–air flow; after displacing upstream slightly, it returned to its original position. The change in the combustion-inducing shock caused by the inhomogeneities was determined to be the leading cause of the ODW displacement and to be the part of the ODW structure most sensitive to disturbances. An underdriven ODW's stability was also tested: it displaced three times as much as its CJ counterpart because of its larger structure. The study of the radical species formation in the induction region of the ODW revealed that HO_2 is the first radical to appear in the induction zone and that the other radicals appear subsequently, near the beginning of the energy release zone together with water. It is therefore difficult to distinguish between the end of the induction period and the start of the energy release period; this is due to the accuracy of the parameters of the combustion model. It was observed that the grid resolution was sufficient to capture the ODW angle and its trends in displacement in the formation and stability simulations. However, the results concerning radical formation showed that the inner ODW structure is still not sufficiently resolved, especially the region delineating the end of the induction period and the beginning of the energy release period. Furthermore, the grid used is not fine enough to capture length scales such as the viscous shock thickness. However, the numerical method used was observed to have grid-convergent behavior in most of the flowfield domain, and the different measures of error calculated for the grid were within acceptable levels for the purposes of this particular study.

Acknowledgment

This work has been supported by the Natural Sciences and Engineering Research Council.

References

[1]Nettleton, M., *Gaseous Detonations: Their Nature and Control*, Chapman and Hall, Bristol, England, U.K., 1987.

[2]Lee, J., "Initiation of Gaseous Detonation," *Annual Review of Physical Chemistry*, Vol. 28, No. 75, 1977, pp. 75–104.

[3]Li, C., Kailasanath, K., and Oran, E., "Detonation Structures Behind Oblique Shocks," *Physics of Fluids*, Vol. 6, No. 4, 1994, pp. 1600–1611.

[4]Kailasanath, K., Oran, E., Boris, J., and Young, T., "Determination of Detonation Cell Size and the Role of Transverse Waves in Two-Dimensional Detonations," *Combustion and Flame*, Vol. 61, Sept. 1985, pp. 199–209.

[5]Shepherd, J., Moen, I., Murray, S., and Thibault, P., "Analyses of the Cellular Structure of Detonations," *21st International Symposium on Combustion*, Combustion Inst., Pittsburgh, PA, 1988, pp. 1649–1658.

[6]Lehr, H. F., "Experiments in Shock-Induced Combustion," *Astronautica Acta*, Vol. 17, Nos. 4–5, 1972, pp. 589–597.

[7]Choi, J. Y., Jeung, I. S., and Yoon, Y., "Computational Fluid Dynamics Algorithms for Unsteady Shock-Induced Combustion, Part 1: Validation," *AIAA Journal*, Vol. 38, No. 7, 2000, pp. 1179–1187.

[8]Matsuo, A., Fujii, K., and Fujiwara, T., "Flow Features of Shock-Induced Combustion Around Projectile Travelling at Hypervelocities," *AIAA Journal*, Vol. 33, No. 8, 1995, pp. 1056–1062.

[9]Wilson, G. J., and Sussman, M. A., "Computation of Unsteady Shock-Induced Combustion Using Logarithmic Species Conservation Equations," *AIAA Journal*, Vol. 31, No. 2, 1993, pp. 294–301.

[10]McClinton, C. R., Raush, D. R., Sitz, J., and Reukauf, P., "Hyper-X Program Status," AIAA Paper 2001-1910, April 2001.

[11]Dudebout, R., Sislian, J. P., and Oppitz, R., "Numerical Simulation of Hypersonic Shock-Induced Combustion Ramjets," *Journal of Propulsion and Power*, Vol. 14, No. 6, 1998, pp. 869–879.

[12]Papalexandris, M. V., "A Numerical Study of Wedge-Induced Detonations," *Combustion and Flame*, Vol. 120, No. 4, 2000, pp. 526–538.

[13]Viguier, C., Figueira da Silva, L., Desbordes, D., and Deshaies, B., "Onset of Oblique Detonation Waves: Comparison Between Experimental and Numerical Results for Hydrogen-Air Mixtures," *26th International Symposium on Combustion*, Combustion Inst., Pittsburgh, PA, 1997, pp. 3023–3031.

[14]Dudebout, R., "Numerical Simulation of Hypersonic Shock-Induced Combustion Ramjet Flowfields," Ph.D. Dissertation, Graduate Dept. of Aerospace Science and Engineering, Univ. of Toronto, Toronto, 1995.

[15]Fusina, G., "Numerical Investigation of Oblique Detonation Waves for a Shcramjet Combustor," Ph.D. Dissertation, Graduate Dept. of Aerospace Science and Engineering, Univ. of Toronto, Toronto, 2003,

[16]Powers, J., and Gonthier, K., "Reaction Zone Structure for Strong, Weak Overdriven and Weak Underdriven Oblique Detonations," *Physics of Fluids A*, Vol. 4, No. 9, 1992, pp. 2082–2089.

[17]Grismer, M., and Powers, J., "Numerical Predictions of Oblique Detonation Stability Boundaries," *Shock Waves*, Vol. 6, No. 3, 1996, pp. 147–156.

[18]Yee, H. C., and Shinn, J. L., "Semi-Implicit and Fully Implicit Shock-Capturing Methods for Nonequilibrium Flows," *AIAA Journal*, Vol. 27, No. 3, 1989, pp. 299–307.

[19]Singh, D., Ahuja, J., and Carpenter, M., "Numerical Simulation of Shock-Induced Combustion/Detonation," *Computing Systems in Engineering*, Vol. 3, Nos. 1–4, 1992, pp. 201–215.

[20]Vlasenko, V., and Sabelnikov, V., "Numerical Solution of Inviscid Flows with Hydrogen Combustion After Shock Waves and in Detonation Waves," AIAA Paper 94-3177, June 1994.

[21]Thaker, A. A., and Chelliah, H. K., "Numerical Prediction of Oblique Detonation Wave Structures Using Detailed and Reduced Reaction Mechanisms," *Combustion Theory Modelling*, Vol. 1, No. 4, 1997, pp. 347–376.

[22]Morris, C. I., Kamel, M. R., and Hanson, R. K., "Expansion Tube Investigation of Ram Accelerator Projectile Flowfields," AIAA Paper 96-2680, July 1996.

[23]Choi, J., Jeung, L., and Yoon, Y., "Numerical Study of Structure and Stability of Oblique Detonation Waves over a 40° Wedge," *27th International Symposium on Combustion*, Combustion Inst., Pittsburgh, PA, 1998.

[24]Li, C., Kailasanath, K., and Oran, E., "Effects of Boundary Layers on Oblique-Detonation Structures," AIAA Paper 93-0450, Jan. 1993.

[25]Viviand, H., "Conservative Forms of Gas Dynamics Equations," *La Recherche Aérospatiale*, No. 1, Jan. 1974, pp. 65–68.

[26]Vinokur, M., "Conservative Equations of Gas-Dynamics in Curvilinear Coordinate Systems," *Journal of Computational Physics*, Vol. 14, Feb. 1974, pp. 105–125.

[27]Parent, B., "Computational Study of Fuel Injection in a Shcramjet Inlet," Ph.D. Dissertation, Graduate Dept. of Aerospace Science and Engineering, Univ. of Toronto, Toronto, 2002.

[28]McBride, B. J., and Reno, M. A., "Coefficients for Calculating Thermodynamic and Transport Properties of Individual Species," NASA TM 4513, Oct. 1993.

[29]Chase, M. W., "JANAF Thermochemical Tables, 3rd ed., Parts I and II," *Journal of Physical and Chemical Reference Data*, Vol. 14, Suppl. 1, 1985.

[30]Dixon-Lewis, G., "Computer Modelling of Combustor Reactions," *Combustion Chemistry*, edited by W. C. Gardiner, Springer-Verlag, New York, 1984, Chap. 2, pp. 21–125.

[31]Anderson, J. D., *Hypersonic and High-Temperature Gas Dynamics*, McGraw–Hill, New York, 1989.

[32]Lutz, A. L., Kee, R. J., Miller, J. A., Dwyer, H. A., and Oppenheim, A. K., "Dynamic Effects of Autoignition Centres for Hydrogen and $C_{1,2}$-Hydrocarbon Fuels," *22nd International Symposium on Combustion*, Combustion Inst., Pittsburgh, PA, 1988, pp. 1683–1693.

[33]Parent, B., and Sislian, J. P., "The Use of Domain Decomposition in Accelerating the Convergence of Quasihyperbolic Systems," *Journal of Computational Physics*, Vol. 179, No. 1, 2002, pp. 140–169.

[34]Roe, P. L., "Approximate Riemann Solvers, Parameter Vectors, and Difference Schemes," *Journal of Computational Physics*, Vol. 43, No. 2, 1981, pp. 357–372.

[35]Jenssen, C. B., and Weinerfelt, P. A., "Parallel Implicit Time-Accurate Navier–Stokes Computations Using Coarse Grid Correction," *AIAA Journal*, Vol. 36, No. 6, 1998, pp. 946–951.

[36]Holden, M. S., and Moselle, J. R., "Theoretical and Experimental Studies of the Shock Wave–Boundary Layer Interaction on Compression Surfaces in Hypersonic Flow," Aerospace Research Lab., Technical Rept. ARL 70-0002, Wright–Patterson AFB, OH, 1970.

[37]Jachimowski, C. J., "An Analytical Study of the Hydrogen–Air Reaction Mechanism with Application to Scramjet Combustion," NASA TP 2791, 1988.

[38]Strauss, W. A., and Scott, J. N., "Experimental Investigation of the Detonation Properties of Hydrogen–Oxygen and Hydrogen–Nitric Oxide Mixtures at Initial Pressures of up to 40 Atmospheres," *Combustion and Flame*, Vol. 19, Aug.–Dec. 1972, pp. 141–143.

M. Sichel
Associate Editor